Bio-Design and Manufacturing (2022) 5:249–264
https://doi.org/10.1007/s42242-021-00180-1

RESEARCH ARTICLE

3D-printed tissue repair patch combining mechanical support and magnetism for controlled skeletal muscle regeneration

Xiaocheng Wang[1] · Ruibo Zhao[2] · Jian Wang[1] · Xinghuan Li[1] · Lijuan Jin[1] · Wenyu Liu[1] · Lifang Yang[3] · Yonghua Zhu[1] · Zhikai Tan[1]

Received: 15 September 2021 / Accepted: 7 December 2021 / Published online: 24 January 2022

Abstract

Physical forces, such as magnetic and mechanical stimulation, are known to play a significant role in the regulation of cell response. In the present study, a biomimetic regeneration patch was fabricated using E-jet 3D printing, which integrates mechanical and magnetic stimulation in a biocompatible "one-pot reaction" strategy when combined with a static magnetic field (SMF). The magneto-based therapeutic regeneration patch induced myoblasts to form aligned and multinucleated myotubes, regulated the expression of myogenic-related genes, and activated the p38α mitogen-activated protein kinase pathway via the initiation of myogenic differentiation. To validate the efficiency of the proposed strategy, the regeneration patch was implanted into mice and exposed to a suitable SMF, which resulted in significantly enhanced in vivo skeletal muscle regeneration. The findings demonstrated that appropriate external physical stimulation provides a suitable biophysical microenvironment that is conducive to tissue regeneration. The method used in the present study represents a promising technique to induce the regeneration of damaged skeletal muscle tissue.

Graphic abstract

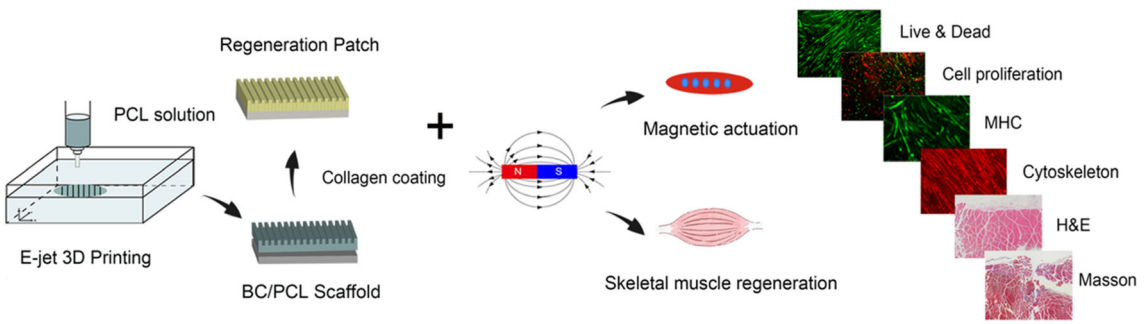

Keywords Functional biomaterials · Magnetic actuation · Myogenic differentiation · Skeletal muscle regeneration · 3D printing

Introduction

Skeletal muscle tissue makes up approximately 40%–45% of the human body's mass, playing a key role in generating body movement and maintaining a contour to the body

Xiaocheng Wang and Ruibo Zhao have contributed equally to this work.

✉ Zhikai Tan
tanzk@hnu.edu.cn

[1] College of Biology, Hunan University, Changsha 410082, China

[2] Department of Orthopaedics, Xiangya Hospital, Central South University, Changsha 410008, China

[3] Key Laboratory of Carcinogenesis and Cancer Invasions of Ministry of Education, School of Basic Medicine Science, Cancer Research Institute, Central South University, Changsha 410008, China

structure [1]. Skeletal muscle tissue generally displays strong self-healing capability; however, muscle defects involving the loss of more than 20% of the original tissue mass cannot be restored by the natural muscle repair mechanism, leading to the formation of chronic functional defects [2]. The current methods of treatment include autologous muscle flap transfer, exercise-based therapies, muscle displacement, dynamic support, etc., but are limited by donor site complications, lack of donor tissue, and other factors [3, 4]. Therefore, bioengineered implantable skeletal muscle constructs capable of the induction of functional neo-tissue formation in vivo would lead to a significant advance in the repair of extensive muscle defects [5, 6].

Skeletal muscle regeneration usually involves the fusion of myoblasts to form polynuclear tubes with diameters in the range 20–100 μm [7]. Myoblast proliferation and myogenic differentiation (myotube formation and myogenic gene expression) are key steps in myogenesis [1]. The orientation of myoblasts is important because freshly recruited cells generate randomly disordered muscle fibers, resulting in scar tissue formation and muscle dysfunction [8]. In addition, the differing responses to mild and severe muscle injuries strongly suggest that a key event in the etiology of volumetric muscle loss injury is the deficiency of considerable numbers of structural cues provided by the extracellular matrix [9, 10]. To re-establish these lost cues, multiple strategies focusing on recapitulating the structural organization of native skeletal muscle have been investigated, especially the uniaxial alignment of muscle cells to enhance the contractile properties of skeletal muscle for effective force generation required for appropriate movement [11–13].

Physical stimulation, including both magnetic and mechanical forces, is known to play a significant role in the regulation of cellular response [14, 15]. Tissues attenuate magnetic fields to only a small degree, and so are able to penetrate deep into tissue, influencing the biochemical processes associated with changes in signaling pathways and cellular events [16]. A magnetic stimulatory event can act as an instructive signal for cell differentiation into a specific cell lineage via the activation of specific signaling pathways [17]. This process is known as magnetic actuation [18]. The p38α mitogen-activated protein kinase pathway (p38α MAPK) is one of many signaling pathways involved in the transformation of physical stimuli to biochemical signals and is a critical regulator in skeletal muscle differentiation [19, 20]. Treatment with the p38α/p38β inhibitor prevents the fusion of myoblasts into myotubes and triggers the induction of muscle-specific genes [21, 22]. More importantly, p38α/p38β is required to activate quiescent satellite cells (muscle stem cells) [22]. Recent studies have also shown that the synergistic effect of static magnetic field and mechanical stimulation can modify cell metabolism [23]. Although many studies have demonstrated the role of physical stimulation in regulating cell behavior, the conclusions of such reports have often been controversial and were based on different experimental conditions, models and hypotheses [24].

Three-dimensional (3D) bioprinting has been extensively employed in the fabrication of bioengineered tissue-specific constructs due to its reproducibility, suitability, and accuracy [25]. In the present study, a patch engineered to induce skeletal muscle regeneration was fabricated using electrohydrodynamic jet (E-jet) 3D printing by accurately printing aligned polycaprolactone (PCL) fibers on a bacterial cellulose (BC) sheet in accordance with a predetermined pattern. The patch was modified with collagen and applied to wound sites to promote myogenic differentiation and guide the ordered formation of tubules in combination with an external static magnetic field (SMF). It was hypothesized that the presence of an SMF and patch would stimulate myoblasts through the activation of mechanosensitive pathways, thereby enhancing myogenic differentiation. The patch not only exhibited excellent biological properties, causing an upregulation of the expression levels of specific factors, but also promoted tissue reconstruction; therefore, it clearly represents a promising method to aid skeletal muscle regeneration.

Materials and methods

Materials

Type I collagen (average molecular weight (Mn) = 2–4 × 10^3 Da) was obtained from Shanghai Ryon Biological Technology Co. Ltd. (Shanghai, China); N,N-dimethylformamide (DMF) was purchased from the Chinese Medicine Group (Beijing, China); PCL pellets (Mn = 1.2×10^5 Da) were acquired from Sigma-Aldrich (USA). Dulbecco's Modified Eagle Medium (DMEM) and fetal bovine serum (FBS) were obtained from Hyclone (Logan, USA); penicillin (100 units/mL) and streptomycin (100 mg/mL) were purchased from Beyotime (Shanghai, China); 40,6-diamidino-2-phenylindole (DAPI), Alexa Fluor 568-phalloidin, Calcein AM, and propidium iodide (PI) were obtained from Yeasen Biological Technology Co., Ltd. (Shanghai, China).

Fabrication of muscle regeneration patch

Bacillus xylinus (ATCC 23,767) colonies were cultured at 30 °C in a specific culture medium prepared by dissolving 5 g of glucose, 1 g of $MgSO_4 \cdot 7H_2O$, 5 g of mannitol, 5 g of polypeptone, 5 g of yeast extract, and 5 mL of ethanol in 1 L of deionized water, then adjusting the final pH to 6.6–7.0. Sheet-type BC scaffolds were obtained after culturing the bacteria for 3–4 weeks, which were rinsed with deionized water to remove any residual medium [26]. They

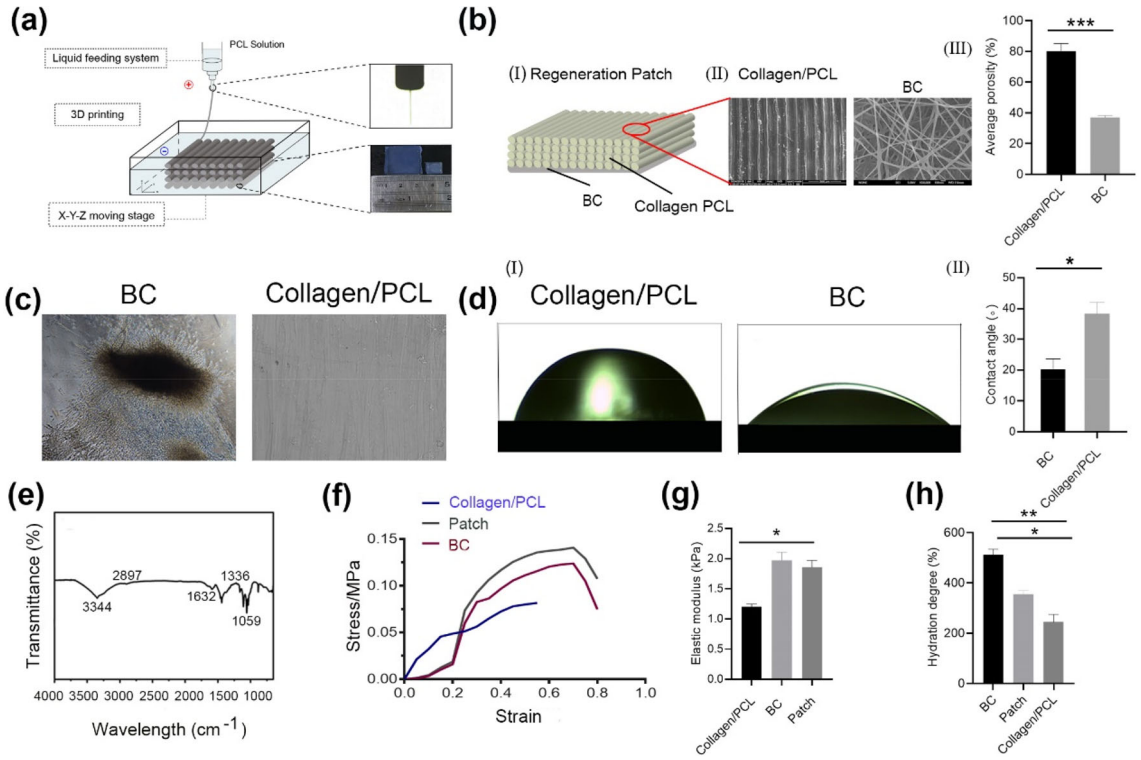

Fig. 1 Schematic illustration of regeneration patch fabrication and its characterization. **a** Schematic diagram of regeneration patch fabrication. **b** Microstructure and porosity of regeneration patch. I. Schematic diagram of double layer structure. II. SEM images of BC and collagen/PCL scaffolds. III. Average porosity of BC and collagen/PCL scaffolds. **c** C2C12 cells seeded on BC and collagen/PCL scaffolds. **d** Water contact angles of BC and collagen/PCL scaffolds. I. Images of measurements. II. Measured contact angles. **e** FTIR spectra of BC. **f** Stress–strain curves. **g** Elastic moduli. **h** Hydration degree of BC, collagen/PCL scaffold, and regeneration patch. $^{*}p < 0.05$, $^{**}p < 0.01$, $^{***}p < 0.001$

were boiled in 1% sodium hydroxide for 30 min and finally rinsed with deionized water. The muscle regeneration patch was fabricated using a customized E-jet 3D printing system consisting of a 3D collection platform, a solution feed, high-voltage power supply, and an observation system [27]. The printing solution was prepared by dissolving PCL pellets in DMF, then stirring at room temperature for 24 h. The resultant solution (8%, w/v) was supplied to a blunt-ended nozzle (27G, ID: 0.21 mm, OD: 0.41 mm). Aligned PCL fibers were accurately printed on the BC scaffold in predetermined patterns (Fig. 1a).

A collagen solution was prepared by dissolving 1 g of collagen powder in 0.1 mol of acetic acid in 1 L of water. The obtained solution was shaken on an oscillator for 15 min until the collagen was completely dissolved. The mixture was then sterilized by passing through a 0.22-μm filter. The regeneration patches were obtained by immersing the 3D-printed BC/PCL scaffolds into collagen solution for 24 h prior to air-drying.

Characterization of muscle regeneration patches

The hydrophilicity of the scaffold materials was tested by the sessile drop method at room temperature using a goniometer and imaging system (SL200KB, Kino). The structure and pore sizes of the scaffolds were characterized by a field emission scanning electron microscope (FE-SEM; Hitachi S-4800) after coating with gold for 60 s. The surface chemistry of the BC scaffolds was evaluated using Fourier transform infrared spectroscopy (FTIR, Nicolet Nexus 670, USA) over the wavenumber range 4000–500 cm^{-1} at a resolution of 2 cm^{-1}. The spectra were further processed and plotted by Opus Origin Pro 9.1 software. The mechanical properties of the specimens were characterized using a Hengyi tensile tester (HY-0230, China) with a 100 N load cell. The porosities of the PCL/collagen and BC scaffold were calculated as follows:

$$\varepsilon = \left(1 - \frac{\rho_{\text{scaffold}}}{\rho_{\text{material}}}\right) \times 100\%,$$

where $\rho_{scaffold}$ represents the density of scaffold, which can be calculated by measuring the volume and mass of scaffold, and $\rho_{material}$ is the density of fiber materials.

In order to assess the water content, the BC scaffold and the regeneration patch were separately immersed into 0.9% sodium chloride solution and kept at 37 °C for 12 h. The hydration degree was calculated as follows:

$$\text{Hydration degree } (\%) = (W_w - W_d)/W_d \times 100\%,$$

where W_d and W_w, respectively, represent the dry weight of the initial samples and the wet weight after soaking.

Cell culture

Mouse-derived myoblasts (C2C12) were purchased from the National Collection of Authenticated Cell Culture (Shanghai, China). The cells were cultured in growth medium (GM) containing 10% FBS and 1% penicillin/streptomycin in an incubator at 37 °C in humid air containing 5% CO_2. The cells (5×10^4 cells/cm^2) were separately seeded on the collagen/PCL and BC scaffolds to assess the biocompatibility of the patch. After 24 h of culture, the cells were visualized using a fluorescence microscope (TI-S; Nikon).

The concentration of FBS was decreased to 3% in differentiation media (DM). The regeneration patches were immersed in 75% ethanol for 12 h, then sterilized by ultraviolet irradiation for 4 h prior to the assessment of differentiation potential. The patches were then placed into 6-well culture plates and seeded at a cell density of 4.0×10^4 cells per well. Tissue culture polystyrene (TCP) was used as control.

Assessment of magnetic field spatial distribution

SMFs are categorized by field intensity, such as ultra-weak (5 μT to 1 mT), weak (1 mT), moderate (1 mT to 1 T), strong (1–5 T), and ultra-strong (>5 T). An SMF of moderate intensity was used in the present study by virtue of its ease of utilization for therapy [28]. A magnet was placed on the cell culture plates to generate the required magnetic field. A Gauss meter (JingFeng, Wenzhou, China; measurement range: 0–200 mT) with a resolution of 0.01 mT, suitable for measuring the far-field distribution of magnetic fields from permanent magnets, was used for magnetic field measurement (the relevant information was presented in Fig. S1 in Supplementary Information). The origin of the magnetic field of the magnet was defined as north (N). The X-axis was plotted parallel to the N pole of the bar magnet. During measurement, the height of the central plane of the bar magnet and the height of the probe were maintained, both horizontally and in a straight line. The components of magnetic induction intensity were measured in three directions. The horizontal and vertical coordinates and magnetic field intensity were recorded using Graphpad Prism software, from which a magnetic induction intensity distribution map of the spatial gradient magnetic field was plotted.

Effect of the regeneration patch and SMF on myoblasts

In order to assess the synergistic effect of the regeneration patch and SMF on myoblasts, C2C12 cells were exposed to a variety of SMFs in the range of 0–20 mT, then stained using a live/dead cell staining kit (Invitrogen, Shanghai, China). The specimens were allocated into four groups depending on the intensity of the applied magnetic field: Patch ($B = 0$ mT), Patch/SMF1 ($B = 2$ mT), Patch/SMF2 ($B = 6$ mT), and Patch/SMF3 ($B = 20$ mT). The TCP without a magnetic field represented the control. The C2C12 cells were cultured with GM (10% FBS) for 24 h prior to exposure to different magnetic fields. The culture medium was changed daily, and the cells were stained after 1 day and 5 days from the start of the experiment.

Assessment of myogenic differentiation

C2C12 cells were cultured on patches for 24 h in GM to assess myogenic differentiation, after which the culture medium was replaced with DM. The cells were then exposed to various SMFs and TCP without SMF representing the control. The culture medium was replaced daily. The differentiation of C2C12 myoblasts cultured with GM was also assessed using the same method.

Immunofluorescent staining, quantitative polymerase chain reaction (q-PCR), and western blot analysis were subsequently performed. Depending on the degree of cell differentiation in each group, the most suitable magnetic field intensity was deduced. The following parameters were quantified by morphological analysis: (1) coverage of myosin heavy chain (MyHC) in the stained myotubes; (2) fusion index (proportion of myotubes with at least three nuclei); (3) rate of maturation (ratio of myotubes with more than five nuclei); (4) orientation factor (orientation degree of the myotubes).

Immunofluorescence staining

Following the myogenic differentiation of C2C12 cells cultured with DM exposed to various SMFs, immunofluorescence staining was conducted to investigate the expressions of vinculin, Ki67 protein, MyHC protein, phospho-p38 protein, and myogenic determination protein (MyOD). The cells were rinsed with phosphate buffer solution (PBS), fixed with paraformaldehyde for 20 min, and then permeabilized with 0.1% Triton X-100. Next, non-specific binding was blocked with sheep serum at 37 °C for 45 min. Each

specimen was incubated with a primary antibody at 4 °C for 12 h. Antibodies against vinculin (1:100; Bioss, bsm-6640R), Ki67 (1:50; Proteintech, 27,309–1-AP), MyHC (1:100; ABclonal, A6935), phospho-p38 (1:100; ABclonal, AP0526), and MyOD (1:100; ABclonal, A0671) were used. After rinsing with PBS, a secondary Alexa Fluor 488 goat anti-rabbit IgG (H + L) was added before incubation for 1 h at room temperature. The samples were rinsed with PBS, 200 μL of 100 nM DAPI were added for 10 min, and were visualized through a fluorescence microscope (TI-S; Nikon). The quantitative analysis was conducted using ImageJ.

Measurement of myoblast p38α MAPK inhibition

The C2C12 cells were seeded (5×10^4 cells/cm^2) onto patches placed in Petri dishes. Two milliliters of GM were added to each Petri dish (to avoid uneven cell seeding caused by floating), which were then incubated for 2–4 h. After the cells had adhered to the patch, GM was replaced with DM, and p38α MAPK inhibitor (SB203580, TargetMol, Shanghai, China) was added as a solution in DMSO at a concentration of 5 μM. Subsequently, the cells were exposed to a specific strength of SMF. The culture medium was exchanged every 24 h. The group with added inhibitor SB203580 was termed SB (+), while the group without the inhibitor was termed SB (−).

Quantitative real-time PCR analysis

After the exposure of samples to various levels of SMF, quantitative real-time PCR (qRT-PCR) was conducted to assess myogenic gene expression levels, namely, MyHC, MyOG, and troponin T1 (Tnnt-1) in C2C12 cells cultured in DM. The cells were digested with trypsin (Solarbio, China) and then rinsed with PBS. The RNA was extracted using an RNAIso Plus kit (Takara, Japan) in accordance with the manufacturer's instructions. A PrimeScript RT reagent kit (Takara, Japan) was used to synthesize cDNA from the RNA, after which qRT-PCR was conducted using a TB Green Premix Ex Taq II kit (Takara, Japan). The expression levels of target genes were normalized to those of the housekeeping genes, GAPDH or β-actin. The primer sequences used for qRT-PCT are detailed in Table S1 in Supplementary Information.

Western blot analysis

Western blot was performed to investigate the potential mechanism of SMF-induced myogenesis. After 6 days of culture, the cells were collected and lysed in lysis buffer. Following the quantification of protein concentration in the lysates using a bicinchoninic acid (BCA) protein assay kit (Beyotime, China), the samples were diluted with lysis buffer to normalize the protein concentration. Each specimen was mixed with loading buffer, boiled at 100 °C for 10 min, and separated by sodium dodecyl sulfate–polyacrylamide gel electrophoresis (SDS-PAGE). The protein bands were transferred electrophoretically to polyvinylidene difluoride (PVDF) membranes. The PVDF membranes were incubated in TBS-T (Tris-buffered saline with 0.1% Tween 20) supplemented with 5% BSA for 40 min at room temperature, followed by incubation overnight at 4 °C with one of the following monoclonal or polyclonal primary antibodies: anti-MyHC (rabbit anti-mouse; 1:1000), anti-MyOD (rabbit anti-mouse; 1:1000), anti-phospho-p38α MAPK (rabbit anti-mouse; 1:1000), anti-p38α MAPK (rabbit anti-mouse; 1:1000), or anti-GAPDH (rabbit anti-mouse; 1:1000). Subsequently, the proteins were stained with a secondary antibody (HRP-conjugated anti-rabbit or anti-mouse) before visualizing using an Odyssey™ infrared imager (LI-COR Biosciences, Lincoln, USA). Finally, quantitative analysis of band intensity was conducted with ImageJ.

Animal experimentation

A tibialis anterior muscle defect was created on the right hind legs of mice to assess the regeneration capability of the experimental patch exposed to an SMF. Briefly, BALB/c mice (20–30 g) were anesthetized with 5% chloral hydrate, and an anterolateral skin incision was made to expose the tibialis anterior muscle in which a cuboid-shaped defect (5 mm × 3 mm × 2 mm in length, width, and depth, respectively) was created. Then, the regeneration patch was implanted over the defect and the wound was closed. A magnetic strip (2 cm × 1.5 cm × 0.5 cm in length, width, and thickness, respectively) capable of generating a suitable SMF was attached over the wound, and the magnetic field intensity was measured using a Gauss meter. The magnetic patch was applied to the wound for 7 days, and then removed. During this period, daily observation was required to prevent the magnetic patch from falling off. The control was represented by the no-treatment group. All procedures were performed in accordance with the regulations approved by the Committee on the Ethics of Animal Experiments of Hunan Provincial Laboratory Animal Center (Permit No. SYXK (Xiang) 2018–0006).

Assessment of muscle regeneration

Skeletal muscle tissue was assessed for wound repair and muscle regeneration by staining sections with hematoxylin & eosin (H&E), Masson's trichrome (MTS), and MyHC. The mice were euthanized after 2 weeks using excess chloral hydrate, the regenerated tissues were harvested, and they were fixed in 4% paraformaldehyde. Muscle tissues were dehydrated using an ascending concentration gradient of ethanol then xylene, embedded in paraffin, and sliced into 5–7 μm sections. To evaluate the histological characteristics

of the regenerated muscle tissue, the parameters of myofiber diameter, total number of centro-nucleated myofibers, area of collagen deposition, and capillary density were measured based on histological images. Freshly formed muscle fibers generally have nuclei at the center of cells when viewed in a cross-section. The hollow red structures in cross-section images were identified as formed capillaries.

Statistical analysis

Each experiment was repeated at least 3 times. Data were expressed as mean ± standard deviation. The results were analyzed statistically through one-way ANOVA using SPSS v25.0 statistical software, followed by a Bonferroni test for multiple comparisons. The differences with p-values < 0.05 were considered significant.

Results

Characteristics of the muscle regeneration patch

An E-jet 3D printing system was employed to accurately print directional PCL fibers on biocompatible BC using predetermined patterns simulating the hierarchical structure and arrangement of in vivo skeletal muscle. Subsequently, the regeneration patch was fabricated by collagen coating (Fig. 1a). The lower layer of the double-layer patch was BC with high biocompatibility, which could provide a barrier against infection, control fluid loss and reduce pain during treatment. In addition, it created and maintained a moist environment in the wound, and absorbed exudates during the inflammatory phase [29]. The upper layer consisted of highly ordered collagen/PCL fibers ranging from 100 to 150 μm in diameter, which were designed to support and guide the proliferation and differentiation of C2C12 cells. The porous nature of the BC and collagen/PCL scaffolds was conducive to the supply of oxygen and nutrients that are essential for cell growth and the maintenance of cell phenotype [30]. The porosity analysis of collagen/PCL and BC scaffolds showed that both of them provided sufficient adhesion sites for cells to adhere to and proliferate (Figs. 1b and 1c). Compared with a collagen/PCL scaffold, the BC was more hydrophilic, with a significant difference in the water contact angle (Fig. 1d). Therefore, the combined BC sheet and collagen/PCL scaffold not only solved the problem of insufficient scaffold thickness, but also increased its hydrophilicity.

The molecular structure of the BC was studied by FTIR. Strong intramolecular and intermolecular hydrogen bonds caused the tensile vibration of hydroxyl groups (O–H), resulting in the appearance of absorption peaks between 3200 and 3500 cm^{-1} in the BC spectra (Fig. 1e). In addition, the spectra exhibited two strong adsorption peaks at 1632 and 1059 cm^{-1}, assigned to acetyl groups and a C=O stretching vibration, respectively [31]. The ideal muscle regeneration scaffold requires appropriate rigidity and elasticity. As shown in Figs. 1f and 1g, the scaffolds were able to withstand strains of 20% to 60%, suggesting that they displayed adequate elasticity and were thus able to endure the mechanical properties required in muscle tension [32]. Water absorption and wettability play an important role in the applicability of biological scaffolds. According to the results displayed in Fig. 1h, both the BC and regeneration patches exhibited very high water compatibility. The results demonstrated that the E-jet 3D-printed tissue regeneration patches provided mechanical support suitable for muscle regeneration.

3D patch and SMF differentiate and orient myoblasts

Myoblasts (C2C12) were seeded on 3D regeneration patches within the wells of 6-well plates, to which varied SMFs were applied. It is of great significance to study the effect of static magnetic field on tissue wound healing and to clarify the spatial distribution of magnetic field in the tissue wound area, so as to standardize the experimental design and operation, as well as to improve the reliability and repeatability of the experiment. Therefore, in this part of the study, we used Ansoft Maxwell-based finite element analysis technology and a Gauss meter to calculate and measure the spatial distribution of magnetic field (Figs. 2a and 2b). The finite element analysis of the magnetic field showed its spatial distribution, and the accurate magnetic field was measured using the Gauss meter (Fig. S1 in Supplementary Information). After the cells were inoculated onto the regeneration patch and exposed to varied SMFs, cell differentiation was observed by cytoskeleton staining after 7 days of culture. The results showed that cells inoculated on the regeneration patch grew in a highly differentiated and directed manner under the action of SMF (Fig. 2c). However, when the magnetic field intensity was greater than 20 mT, the muscle tubes formed by cell differentiation were deformed, which was not conducive to the regeneration of skeletal muscle. Therefore, for the in vitro experiments, we mainly explored the effect of SMF less than 20 mT on the biological behavior of myoblasts.

3D patches promote the growth and adhesion of myoblasts

C2C12 cells were inoculated on 3D regeneration patches and exposed to a specific SMF (< 20 mT), with cells cultured on TCP used as control (Fig. 3a). Live/dead cell staining was performed to evaluate the viability of myoblasts in DM and GM at day 1 and day 5. The results demonstrated that the cells were mostly live (green) following exposure to SMFs for 1 day, with only a few dead cells (red) irrespective of the

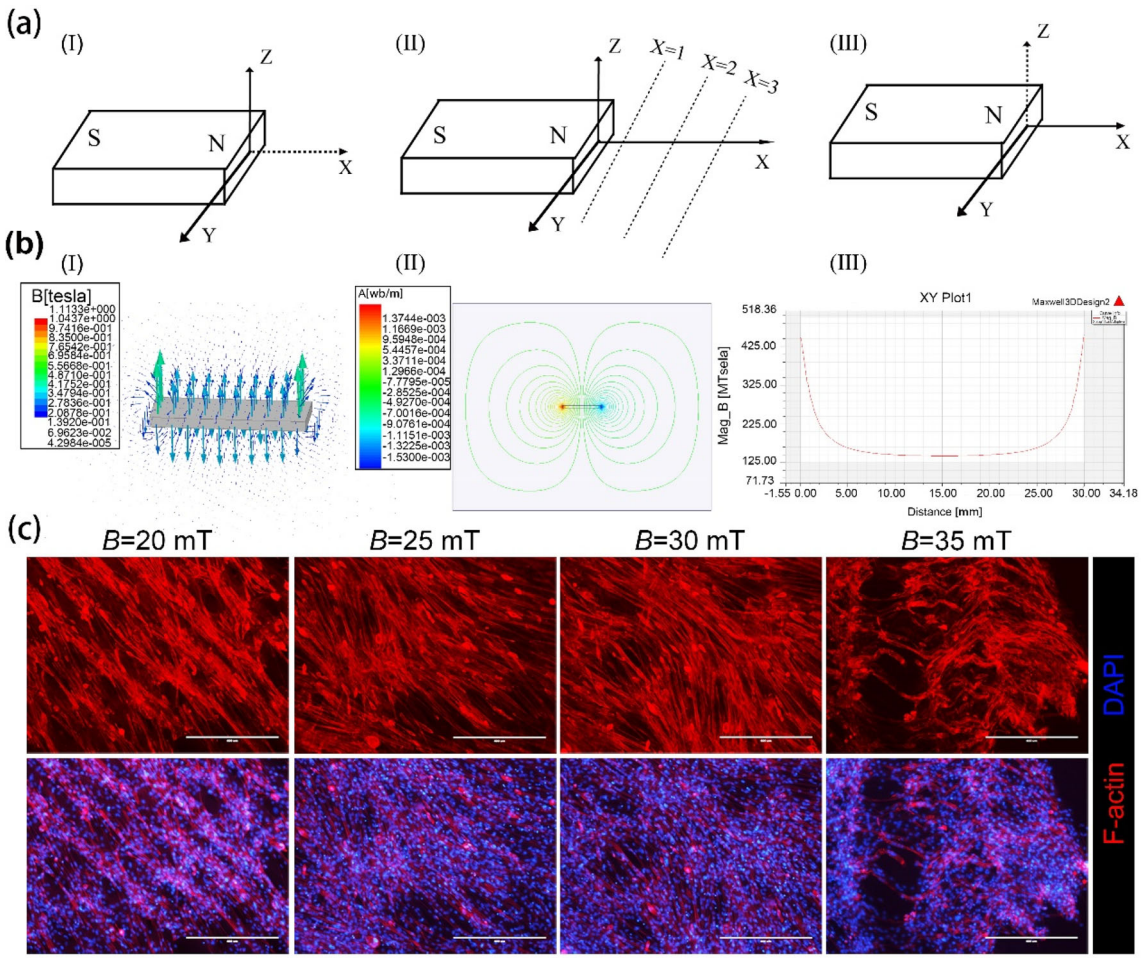

Fig. 2 Effects of regeneration patches and SMFs on the differentiation and arrangement of myoblasts. **a** Schematic illustration of the measurement of magnetic fields. **b** Finite element analysis method in Ansoft Maxwell was used to simulate the spatial distribution of SMFs. **c** Representative immunofluorescent images showing the cytoskeleton (F-actin: red) and cell nuclei (DAPI: blue) under varied SMFs, scale bar = 400 μm

culture medium used (GM or DM), indicating that neither the magnitude of magnetic field strength nor serum concentration in the medium influenced the cell viability. After 5 days, the number of living cells in each group was significantly increased, indicating that the cells had proliferated rapidly (Figs. 3b and 3c; Figs. S2a and S2b in Supplementary Information). At this time, the viability of C2C12 cells exposed to SMFs was greater compared with those in the control and patch only groups, suggesting that an adequate magnetic field enhanced myoblast activity. The adhesion of C2C12 cells in each group was assessed using vinculin staining after incubation in GM for 24 h (Figs. 3d and 3e). The results indicated that the adhesion of cells to scaffolds in the Patch/SMF1 (B = 2 mT) group was the greatest. In addition, C2C12 cells were stained for Ki67 following culture in GM for 1 and 5 days (Figs. 3f and 3g; Figs. S2c and S2d in Supplementary Information). The cell proliferation in the SMF treatment groups was greater than those in other groups; especially in the Patch/SMF1 (B = 2 mT) group, cell proliferation was approximately 10% higher. The above results demonstrate that the regeneration patch displayed excellent biocompatibility, and, in combination with an appropriate magnetic field (SMF1), cell proliferation and adhesion were enhanced.

Myogenic differentiation analysis

The influence of the patch and SMFs on the myogenic differentiation of C2C12 cells was assessed for parameters including myotube formation and myogenic marker expression. The results indicated that after 3 days of culture, myotube formation, a marker of myoblast differentiation, was observed in all groups. Compared with the control, the patch with SMF induced the formation of more myotubes. At day 5, the number of myotubes was significantly greater,

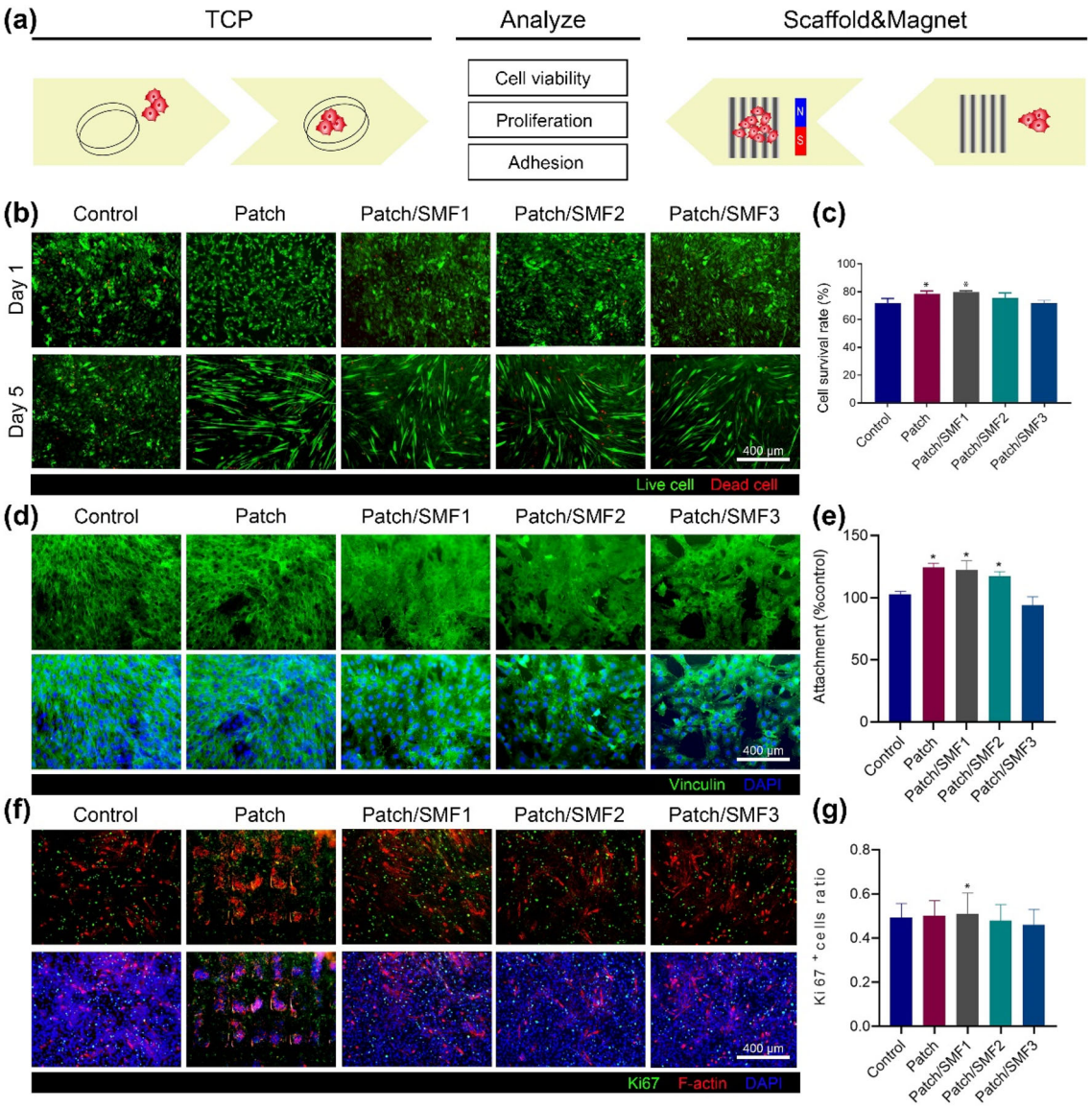

Fig. 3 Effects of regeneration patches and SMFs on myoblasts' viability, adhesion and proliferation. **a** Schematic illustration describing the effects of 3D culture and magnetic stimulation on cell viability, proliferation, and adhesion compared with 2D culture (TCP). **b** Fluorescent images demonstrating live/dead staining of C2C12 cells on day 1 and day 5 after culture in medium with 10% FBS (GM) and exposure to various SMFs (live cells: green; dead cells: red; Patch ($B = 0$ mT), Patch/SMF1 ($B = 2$ mT), Patch/SMF2 ($B = 6$ mT), or Patch/SMF3 ($B = 20$ mT)). **c** Quantification of C2C12 cell viability in GM based on (**b**) at day 5. **d** Immunofluorescence images of myoblasts cultured under varied SMFs for 1 day (vinculin, green; DAPI, blue). **e** Quantification of cell adhesion based on (**d**). **f** Ki67 + immunofluorescence showing C2C12 proliferation on day 1 after culture in DM and exposure to various SMFs. **g** Quantification of C2C12 cell proliferation in DM after 1 day based on (**f**). $^{*}p < 0.05$

and the Patch/SMF1 ($B = 2$ mT) group exhibited superior myotube morphology compared with other groups. After culture for 7 days, myoblasts in all groups were found to be highly differentiated (Fig. 4a). Compared with the control, the regeneration patch increased the cellular orientation, while the exposure to SMF resulted in significantly greater multinucleated myotube formation (differentiation rate, Fig. 4b). The statistical analysis demonstrated that formed myotubes in the Patch/SMF1 group displayed a significantly higher maturation rate, fusion index, and length compared with the control (Figs. 4c–4g). To further verify the effect of magnetic field and exclude the potential effects of low serum level on cell differentiation, cells were cultured with GM and their differentiation was observed after culture for 7 days (Fig. S3 in Supplementary Information). The cells in the patch groups were arranged satisfactorily, while the SMFs resulted in significantly higher multinucleated myotube formation. Compared with other groups, the

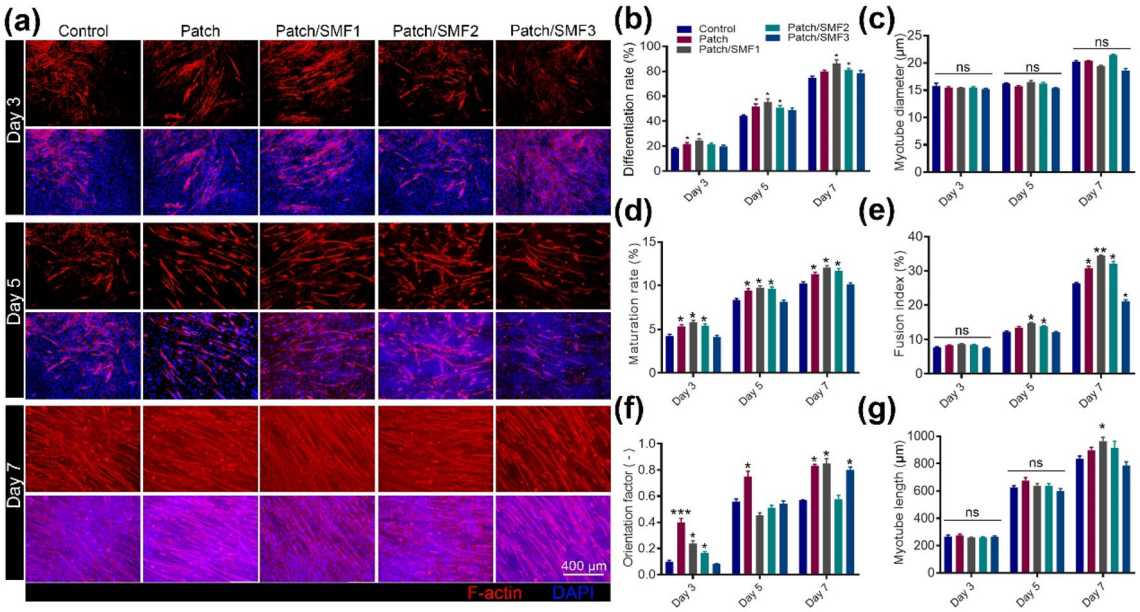

Fig. 4 Synergistic effects of SMFs and regeneration patches on the myogenic differentiation of myoblasts after incubation in DM. **a** Myogenic differentiation of C2C12 cells on patches exposed to various SMFs (Patch ($B = 0$ mT), Patch/SMF1 ($B = 2$ mT), Patch/SMF2 ($B = 6$ mT), or Patch/SMF3 ($B = 20$ mT)), based on the immunofluorescence staining of F-actin (red)/DAPI (blue). **b** Differentiation rate (%). **c** Myotube diameter (μm). **d** Maturation rate (%). **e** Fusion index (%). **f** Orientation factor. **g** Myotube length (μm) of myoblasts. $^{*}p < 0.05$, $^{**}p < 0.01$, $^{***}p < 0.001$

Patch/SMF1 group exhibited the highest rate of differentiation.

The gene expression levels of myogenic markers (MyOG, MyHC, and Tnnt-1) were determined using qRT-PCR as a measure of the myogenic differentiation of C2C12 cells exposed to a variety of SMFs. At day 3, myogenic gene expression in all groups was greater than that in the control, and that in the Patch/SMF1 group (1.8–2.5-fold) was greater than that in other groups (1.5–1.8-fold) (Fig. 5a). In particular, genes related to myogenic differentiation were significantly upregulated in the patch groups, demonstrating the role of alignment in promoting myoblast differentiation. As the differentiation of myoblasts progressed, the related genes were upregulated. After incubation for 5 days in DM, the C2C12 cells exposed to SMFs displayed significantly higher gene expression than the control group. Of all groups, the Patch/SMF1 group exhibited the highest myogenic gene expression (Fig. 5b). By day 7 of differentiation, the gene expression levels for MyHC, MyOG, and Tnnt-1 in the Patch/SMF1 group remained higher compared to other groups (Fig. 5c). These results consisted an additional demonstration that the patch combined with SMF significantly promoted the myogenic differentiation of myoblasts through the upregulation of genetic markers MyHC, MyOG, and Tnnt-1. As the Patch/SMF1 group demonstrated the greatest performance in terms of myogenic differentiation in vitro, it was used to study the mechanism of the process in subsequent experiments.

Mechanisms of myogenic differentiation

In order to assess whether the inhibition of p38α MAPK signaling pathway was rate-limiting for myoblast differentiation, the differentiation capability of C2C12 cells was assessed by culture in DM and exposure to SMF1 ($B = 2$ mT) for 7 days to induce full differentiation, either in the presence or absence of SB203580 (SB). The myogenic gene expression levels of MyHC, MyOG, and Tnnt-1 decreased significantly in all groups after incubation in DM in which SB had been added (Figs. 5d–5f), as compared with those cultured without SB. The expression levels of MyOG were significantly higher in the Patch/SMF1 group at an early stage, suggesting the active regulation of myogenic differentiation (Fig. 5d). Compared with other groups, the Patch/SMF1 group also demonstrated significantly higher levels of myogenic gene expression, including MyHC and Tnnt-1 (Figs. 5e and 5f). The results demonstrated that the positive influence of SMF on myogenesis was blocked by the addition of the p38α inhibitor, SB. Hence, the p38α MAPK signaling pathway was proved to be important in myogenic differentiation when exposed to particular magnetic field strengths.

The immunofluorescent staining of MyHC was performed to further investigate the differentiation of C2C12 cells when cultured in DM with SB. After 7 days, the number, length, and diameter of myotubes decreased significantly in all groups (Fig. 6a). Nevertheless, after removal of SB from the

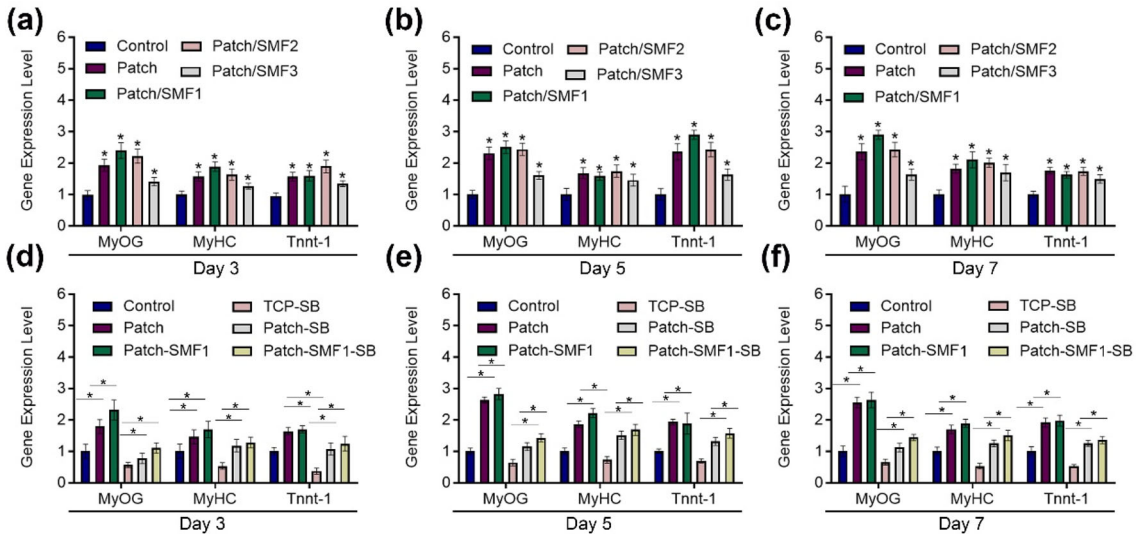

Fig. 5 RT-PCR analysis of gene expression of the myogenic markers (MyOG, MyHC, and Tnnt-1) in C2C12 cells after exposure to SMFs (Patch ($B = 0$ mT), Patch/SMF1 ($B = 2$ mT), Patch/SMF2 ($B = 6$ mT), or Patch/SMF3 ($B = 20$ mT)). Culture in DM (3% FBS) for **a** 3, **b** 5, and **c** 7 days. **d**–**f** Gene expression of myogenic markers in C2C12 cells in the presence or absence of SB after exposure to SMF for **d** 3, **e** 5, or **f** 7 days. $^{*}p < 0.05$

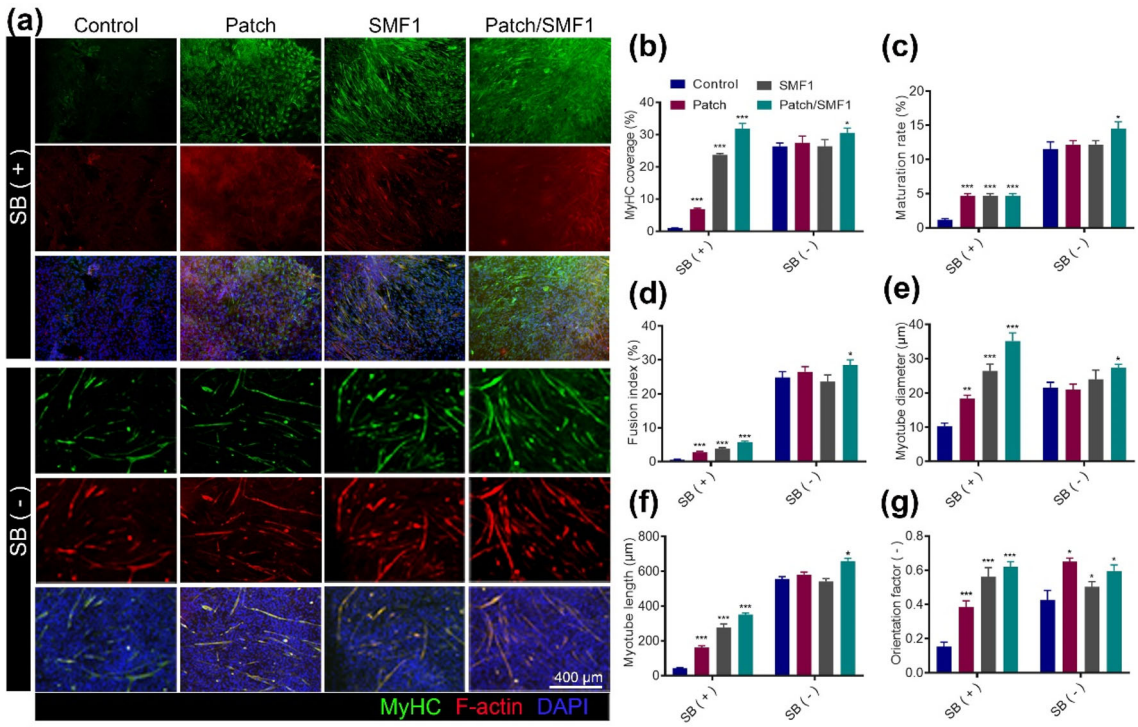

Fig. 6 Immunofluorescence staining of MyHC in myoblasts cultured in DM with the p38α MAPK inhibitor, SB. **a** Immunofluorescence staining of MyHC protein (green)/F-actin (red)/DAPI (blue) in C2C12 cells. **b**–**g** Quantification of myotube formation: **b** MyHC coverage (%); **c** Maturation rate (%); **d** Fusion index (%); **e** Myotube diameter (μm); **f** Myotube length (μm); **g** Orientation factor. $^{*}p < 0.05$, $^{**}p < 0.01$, $^{***}p < 0.001$

culture medium and exposure to SMF for 7 days, numerous myotubes of greater length and diameter were formed. The number, diameter, length, maturation index, and coverage of myotubes were quantified by morphological analysis

(Figs. 6b–6g). The results indicated clear differences in all groups with the Patch/SMF1 group showing the highest maturation rate, while cells in the control group had barely differentiated.

Western blot was performed to analyze whether the expression of myogenic marker proteins during the myogenic differentiation of myoblasts was related to the p38α MAPK signaling pathway. When C2C12 cells were cultured in DM without SB, significantly higher MyHC, MyOD, and phospho-p38α (p-p38α) protein expression was observed compared with the control (Fig. 7a). Furthermore, protein expression levels in the Patch/SMF1 group were higher than those in other groups. In the presence of SB, no apparent change in total p38α expression was detected, while the expression of MyHC, MyOD, and phospho-p38α proteins in all groups decreased significantly (Figs. 7b and 7c). The immunofluorescent staining of phospho-p38α and MyOD proteins also illustrated that protein expression decreased significantly in the presence of SB (Figs. 7d and 7e). These results indicated that SMFs regulate myogenic differentiation via the p38α MAPK signaling pathway (Fig. 8).

In vivo muscle regeneration

Aimed at further investigating the process of skeletal muscle regeneration of the regeneration patch combined with SMF in vivo, a mouse tibialis anterior muscle defect model was established. The 3D regeneration patch was immersed in PBS and then implanted subcutaneously into mice. After closing the wound, a magnetic strip capable of generating a suitable SMF (SMF1 = 2 mT) was placed close to the wound (Fig. 9a) for a week, after which it was removed (Fig. S4a in Supplementary Information). The mice were allocated into four groups, namely, SMF1, Patch, Patch/SMF1, and non-treated (representing the control group). Gross appearance, MTS, and H&E were recorded after implantation for 2 weeks to assess the skeletal muscle regeneration. In the Patch/SMF1 ($B = 2$ mT) and Patch groups, the wound defect was almost completely filled with new tissue, and the transplanted area could not be distinguished from the surrounding natural muscle except the position of suture. The non-treated and SMF1 groups still showed obvious defects even 2 weeks after implantation. In the Patch/SMF1 and Patch groups, H&E staining of the cross-sections of healed areas showed that a large number of cells had infiltrated into the scaffold with the deposition of a large amount of new extracellular matrix (ECM) while cell infiltration and new ECM formation were very limited in the control and SMF1 groups. This was further confirmed by Masson trichrome staining, showing that the remaining high-density collagen was located on the defect surface. In contrast, only a small fraction of collagen fibers were dispersed and deposited at the defect area treated with Patch/SMF1 (Figs. 9b, 9c, and 9g). The freshly formed muscle fibers had their nuclei at the center of the cross-sections, while hollow, red structures observed in cross-section were identified as formed capillaries. Compared with the non-treated and SMF1 groups, the number of centro-nucleated myofibers was significantly increased in the Patch/SMF1 and Patch groups, especially in the Patch/SMF1 group (Fig. 9d). The capillary density around the area of fibrosis was also significantly greater in the Patch/SMF1 group compared with other groups, which was close to the vascular density in the defect area (Fig. 9e). There were no significant differences in the diameter of myofibers among the groups (Fig. 9f). Furthermore, after staining patches were retrieved from mice, it was found that a large number of cells had infiltrated into the BC scaffold, demonstrating that the regeneration patch exhibited excellent biocompatibility (Fig. S4 in Supplementary Information). In summary, the results above demonstrated that the regeneration patch exposed to a suitable intensity of SMF enhanced skeletal muscle regeneration in vivo.

Discussion

Physical signals in the micro-environment surrounding cells directly affect their behavior by sensing the micro- and nanoscale environmental changes through surface receptors and transmitting those signals internally, which influences their growth, elongation, migration, and differentiation [33–35]. Therefore, it has been recognized that suitable physical stimulation is required in the design and development of biomaterial systems for tissue engineering [34]. Recent advances in tissue engineering have enabled the fabrication of tissue constructs that recapitulate the organization of native skeletal muscle containing aligned multinucleated muscle cells with contractile function [36, 37]. For bioengineered skeletal muscle structures to successfully restore impaired muscle function in vivo, it is imperative that the myogenic differentiation of myoblasts is rapidly achieved. This is because satellite cells respond to injury, become activated, proliferate, subsequently differentiate into myoblasts during skeletal muscle repair, and then fuse to form muscle fibers integrating into muscle tissue [38]. However, the scale and severity of damage that can be effectively repaired by satellite cell activation are somewhat limited. In addition, random skeletal muscle fiber arrangement disorder may occur during the process of muscle tissue repair [39]. Thus, the development of a strategy using suitable implants to accelerate myogenic differentiation is of considerable importance [40].

At present, relatively few methods exist in which myogenic differentiation is accelerated in parallel with the formation of ordered myotubules. Although there have been reports of designed aligned fiber-based stents or magnetic fields used for tissue engineering [8, 41], the combination of

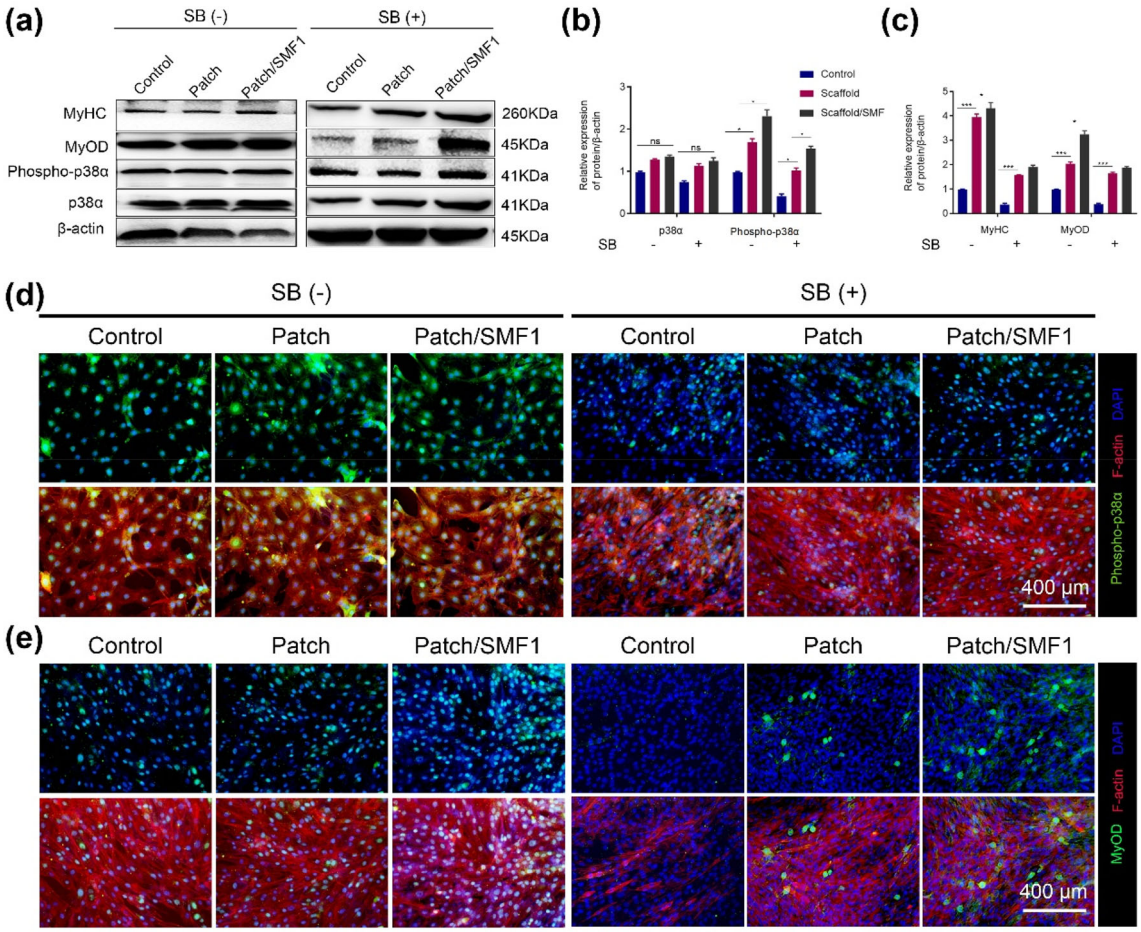

Fig. 7 Western blot analysis of relevant protein expressions (MyHC, MyOD, Phospho-p38α, and p38α) in myoblasts treated with regeneration patches and exposed to SMF (SMF1 = 2 mT) for 7 days in DM with (+) or without (−) SB. **a** Western blot analysis of MyHC, MyOD, phospho-p38α, and p38α in various groups. **b** Relative protein expression levels of p38α and phospho-p38α. **c** Relative protein expression levels of MyHC and MyOD. **d** Immunofluorescent staining of phospho-p38α protein (green)/F-actin (red)/DAPI (blue). **e** Immunofluorescent staining of MyOD protein (green)/F-actin (red)/DAPI (blue). $^{*}p < 0.05$, $^{**}p < 0.01$, $^{***}p < 0.001$

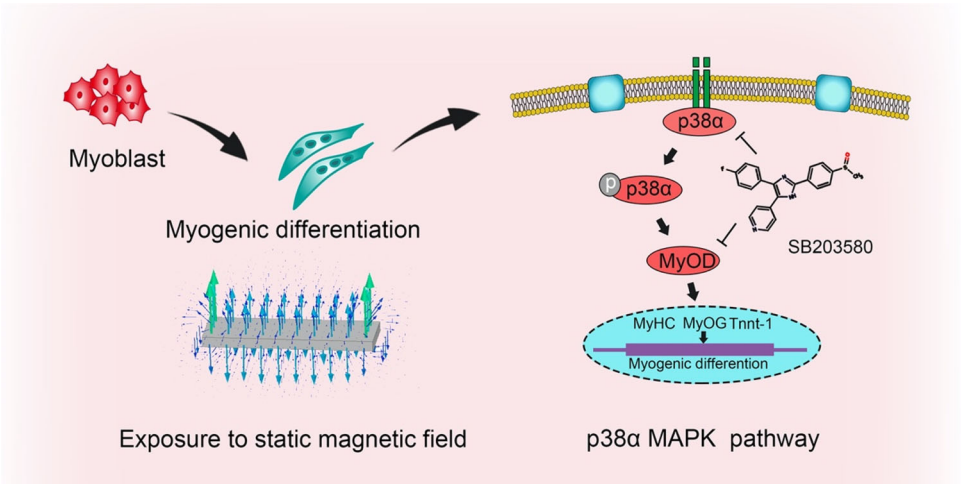

Fig. 8 Schematic illustration describing the mechanism of myogenic differentiation in myoblasts exposed to SMF

the two for the promotion of skeletal muscle repair has not been presented. In the current study, we developed a "one-pot reaction" strategy in which a 3D-printed regeneration patch combined with a suitable SMF greatly induced myoblast

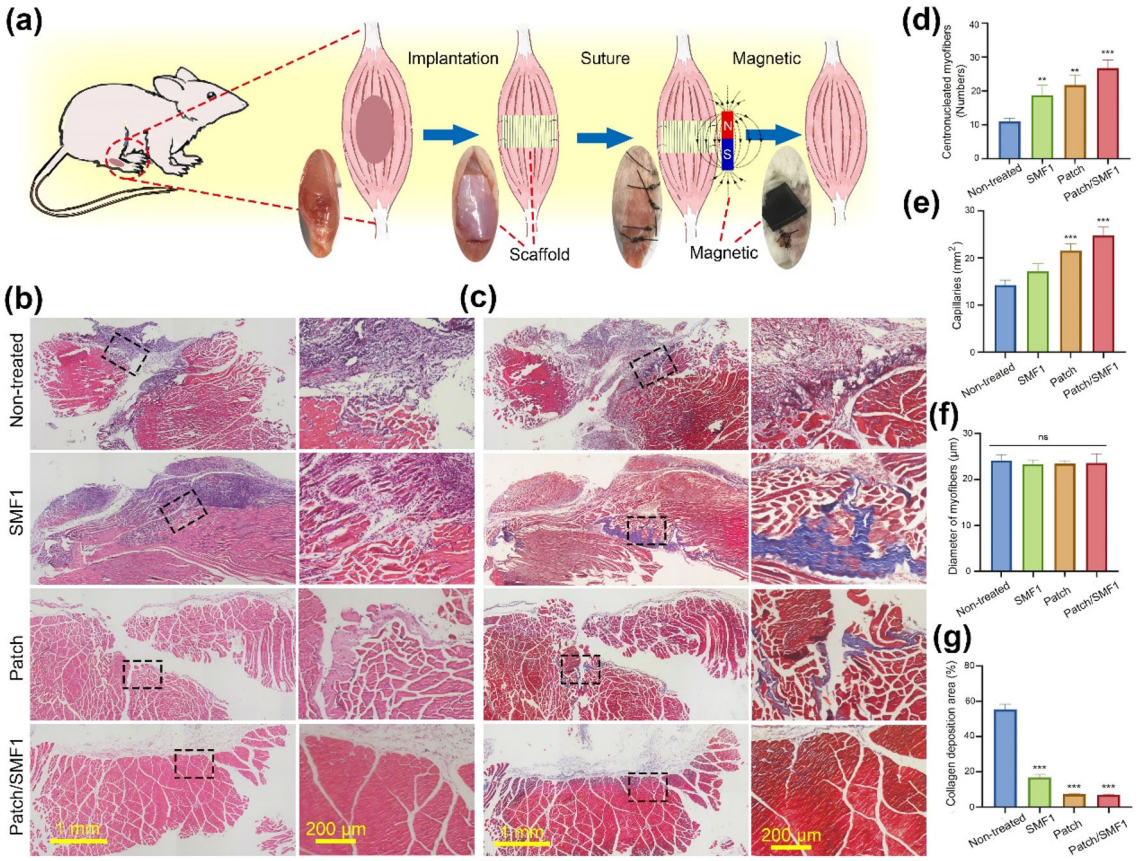

Fig. 9 Skeletal muscle healing and regeneration after treatment with the regeneration patch and SMF. **a** Schematic illustration describing the experimental animal procedure in BALB/c mice. **b** Representative histological slides stained with H&E. Dashed lines: defect, scale bar = 1 mm (right: Magnified image of the area bounded by the yellow dashed line, scale bar = 200 μm); **c** Representative histological slides stained with Masson's trichrome, scale bar = 1 mm. Dashed lines: defect (right: Magnified image of the area bounded by the yellow dashed line, scale bar = 200 μm). **d** Number of regenerating myofibers (centro-nucleated myofibers). **e** Capillary density close to the defect site. **f** Diameter of myofibers surrounding the defect in all groups. **g** Quantification of area of collagen deposition (%) based on (**c**). $^{*}p < 0.05$, $^{**}p < 0.01$, $^{***}p < 0.001$

alignment and differentiation, thus accelerating skeletal muscle repair. Upon investigating the mechanism of myogenic differentiation during this process, it was shown that the aligned fibers of the patch mimicked the anisotropic structure of the elongated muscle fibers of skeletal muscle, providing vital cues for morphogenesis [42]. In addition, the patch was modified with collagen, the main component of skeletal muscle ECM, which can be electrospun with synthetic polymers such as polylactic acid (PLLA) and polycaprolactone (PCL) to prepare fiber pads with high biocompatibility. The results indicated that these pads promoted cell adhesion and provided better mechanical properties for tissue repair [43, 44]. Contact guidance cues (ranging from nanometer to micron-scale) stimulated a variety of myoprogenitor cell populations and resulted in enhanced functional outcomes, including regulated cytoskeletal alignment, striated myotubule formation and myogenic expression, as compared with the control groups. The preparation of the regeneration patch was cost-effective and experimentally feasible, requiring neither expensive materials nor complicated procedures. The 3D-printed regeneration patch was combined with an SMF to promote cell attachment, forming differentiated myotubes that were significantly longer compared with those formed in the 2D culture. Aligned PCL fibers combined with the BC sheet-scaffold resulted in a patch with anisotropic mechanical properties, possibly better suited to handling the stresses experienced in native skeletal muscle [30]. Moreover, the muscle precursor cells were constrained to be highly aligned with the 3D-printed structure and to compact due to limited space, resulting in the superior orientation of regenerating myotubes, more closely mimicking the morphology and organization of natural muscles.

Physical stimulation, growth factors, and the physicochemical properties of scaffolding materials are important modulators of cell proliferation and differentiation, which can control tissue regeneration in vivo. Among various exter-

nal physical stimuli, magnetic fields have recently been the focus of considerable attention, exhibiting a broad potential for applications such as increased osteogenic differentiation, angiogenesis, and bone regeneration [45–47]. Magnetotherapy provides a non-invasive, safe, and easy-to-use method for the treatment of sites of injury, sources of pain and inflammation, as well as other diseases. In addition, in terms of clinical therapy, this technique has advantages in a number of application areas [48]. A permanent magnet can easily be used for tissue stimulation without the need for a power supply device, making SMF stimulation feasible for long-term tissue healing. The regulation of cellular behavior varies among different intensities of magnetic field [49]. Therefore, we investigated the influence of various SMFs on myogenic differentiation. The results demonstrated that the proliferation, differentiation, and long-term survival of skeletal muscle cells can be improved at a magnetic field intensity of 2 mT. However, reduced myofibril formation and disordered myotubule formation were observed at a magnetic field intensity > 20 mT. Based on these findings, this optimal magnetic field strength was exploited in combination with a regeneration patch to act on myoblasts, which resulted in greater cellular activity and accelerated myogenic differentiation.

The molecular mechanisms of magnetic induction include activation of the Wnt/β-Catenin and integrin signaling pathways (including focal adhesion kinase, paxillin, RhoA, MAPK, and NF-κB) [16, 50]. The present study demonstrated that SMFs promote the expression of MyOD during the myogenic differentiation of myoblasts. MyOD is a critical factor for the initiation of myogenic differentiation and the subsequent expression of myogenic markers, such as Tnnt-1, MyOG, and MyHC [51]. As p38α MAPK is related to both myogenic differentiation and the transduction of mechanical/biochemical signals [52], there is a very strong possibility that SMFs mediate the regulation of the MyOD gene and myogenesis via the p38α MAPK pathway. Western blot was used to measure the expression of p38 MAPK signaling pathway-related proteins and myogenic marker proteins of myoblast differentiation. In the absence of SB, the Patch/SMF1 group displayed significantly higher myogenic protein expression than other groups. However, the protein expression levels of phospho-p38α and MyOD in all groups reduced significantly after cells were incubated with DM supplemented with SB, although no apparent change in total p38α expression was observed. These data further established that the patch combined with SMF had regulated myogenic differentiation via p38α MAPK and increased the levels of phospho-p38α.

In order to validate the synergistic regeneration capability of SMF and the regeneration patch, the latter was implanted subcutaneously into mice, and an optimal strength of magnetic field was applied to the wound. The outcomes indicated effective muscle fiber formation, resulting in the accelerated restoration of muscle function, as confirmed by the reduction in collagen deposition and increased number of fresh muscle fibers. In our previous research, we demonstrated that collagen scaffolds with aligned fibers could guide the formation of ordered myotubules, which was beneficial for the reduction of scar tissue formation and muscle dysfunction [53]. Therefore, we anticipated that the deposition of collagen in the patch of the SMF group would be less than that in the other groups, which was confirmed by the greater number of new muscle fibers and reduced collagen deposition in the Patch/SMF1 group. The number of new muscle fibers in both the patch only and the SMF only groups were not significantly different from each other, indicating that the synergistic use of patch and SMF has substantial potential in skeletal muscle repair. In addition, cells could be actuated by temporary magnetic stimulation prior to implantation, which consists a safer and more practical way to produce functional tissue engineered constructs.

Although the present study provides promising data on the development of a novel therapeutic option for reconstructive surgery, many challenges still need to be overcome. For example, vascularization is a critical aspect of skeletal muscle regeneration. It is of high significance to promote vascularization at the site of injury to overcome the limitations of diffusion of oxygen and nutrients, and to maintain cell survival and function [54]. Although previous studies have confirmed that SMF is able to promote an angiogenic response in endothelial cells, including the gene expression of vascular endothelial growth factor and angiogenin-1, as well as capillary and blood vessel formation [45, 55], future studies will need to investigate the role of SMF in promoting angiogenesis in skeletal muscle repair.

Conclusions

The present study developed a regeneration patch using E-jet 3D printing, which proved successful in biochemically and topographically mimicking skeletal muscle constructs in vivo. Through utilization of this patch along with a suitable magnetic field, myoblasts were induced to form aligned and multinucleated myotubes. Magnetic stimulation activated the p38α MAPK signaling pathway that played an important role in the myogenic differentiation of myoblasts. In addition, static magnetic field combined with the regeneration patch significantly enhanced skeletal muscle regeneration in vivo. The results demonstrated that appropriate external physical stimulation provides a suitable biophysical microenvironment that is conducive to tissue regeneration. The proposed technology can pave the way for potential therapeutic tools in

the future for the effective regeneration of damaged skeletal muscle tissue.

Supplementary Information The online version contains supplementary material available at https://doi.org/10.1007/s42242-021-00180-1.

Acknowledgements This study was financially supported by the Natural Science Foundation of Hunan Province (No. 2019JJ40018), and Hunan University (No. 53112102).

Author contributions XW and RZ were involved in conceptualization, data curation and formal analysis; JW, XL, LJ, WL, LY and YZ helped in investigation and methodology; ZT was involved in validation, writing and editing.

Declarations

Conflict of interest The authors declare that they have no conflict of interest.

Ethical approval All institutional and national guidelines for the care and use of laboratory animals were followed.

References

1. Zhu M, Li W, Dong XH et al (2019) In vivo engineered extracellular matrix scaffolds with instructive niches for oriented tissue regeneration. Nat Commun 10(1):4620. https://doi.org/10.1038/s41467-019-12545-3
2. Corona BT, Wenke JC, Ward CL (2015) Pathophysiology of volumetric muscle loss injury. Cells Tissues Organs 202:180–188. https://doi.org/10.1159/000443925
3. Carnes ME, Pins GD (2020) Skeletal muscle tissue engineering: biomaterials-based strategies for the treatment of volumetric muscle loss. Bioengineering 7(3):85. https://doi.org/10.3390/bioengineering7030085
4. Farr AC, Hogan KJ, Mikos AG (2020) Nanomaterial additives for fabrication of stimuli-responsive skeletal muscle tissue engineering constructs. Adv Healthcare Mater 9:e2000730. https://doi.org/10.1002/adhm.202000730
5. Grasman JM, Zayas MJ, Page RL et al (2015) Biomimetic scaffolds for regeneration of volumetric muscle loss in skeletal muscle injuries. Acta Biomater 25:2–15. https://doi.org/10.1016/j.actbio.2015.07.038
6. Kwee BJ, Mooney DJ (2017) Biomaterials for skeletal muscle tissue engineering. Curr Opin Biotechnol 47:16–22. https://doi.org/10.1016/j.copbio.2017.05.003
7. Jana S, Leung M, Chang J et al (2014) Effect of nano- and microscale topological features on alignment of muscle cells and commitment of myogenic differentiation. Biofabrication 6(3):035012. https://doi.org/10.1088/1758-5082/6/3/035012
8. Yeo M, Kim G (2020) Micro/nano-hierarchical scaffold fabricated using a cell electrospinning/3D printing process for co-culturing myoblasts and HUVECs to induce myoblast alignment and differentiation. Acta Biomater 107:102–114. https://doi.org/10.1016/j.actbio.2020.02.042
9. Kasukonis BM, Kim JT, Washington TA et al (2016) Development of an infusion bioreactor for the accelerated preparation of decellularized skeletal muscle scaffolds. Biotechnol Progr 32:745–755. https://doi.org/10.1002/btpr.2257
10. Quarta M, Cromie M, Chacon R et al (2017) Bioengineered constructs combined with exercise enhance stem cell-mediated treatment of volumetric muscle loss. Nat Commun 8:15613. https://doi.org/10.1038/ncomms15613
11. Jenkins TL, Little D (2019) Synthetic scaffolds for musculoskeletal tissue engineering: cellular responses to fiber parameters. npj Regenerat Med 4:15. https://doi.org/10.1038/s41536-019-0076-5
12. Salimath AS, Garcia AJ (2016) Biofunctional hydrogels for skeletal muscle constructs. J Tissue Eng Regenerat Med 10:967–976. https://doi.org/10.1002/term.1881
13. Barrett P, Quick TJ, Mudera V et al (2020) Generating intrafusal skeletal muscle fibres in vitro: current state of the art and future challenges. J Tissue Eng 11:1–15. https://doi.org/10.1177/2041731420985205
14. Santos LJ, Reis RL, Gomes ME (2015) Harnessing magnetic-mechano actuation in regenerative medicine and tissue engineering. Trends Biotechnol 33:471–479. https://doi.org/10.1016/j.tibtech.2015.06.006
15. Antman-Passig M, Giron J, Karni M et al (2021) Magnetic assembly of a multifunctional guidance conduit for peripheral nerve repair. Adv Funct Mater 31:2010837. https://doi.org/10.1002/adfm.202010837
16. Yun HM, Ahn SJ, Park KR et al (2016) Magnetic nanocomposite scaffolds combined with static magnetic field in the stimulation of osteoblastic differentiation and bone formation. Biomaterials 85:88–98. https://doi.org/10.1016/j.biomaterials.2016.01.035
17. Wang Q, Chen B, Cao M et al (2016) Response of MAPK pathway to iron oxide nanoparticles in vitro treatment promotes osteogenic differentiation of hBMSCs. Biomaterials 86:11–20. https://doi.org/10.1016/j.biomaterials.2016.02.004
18. Li Y, Ye D, Li M et al (2018) Adaptive materials based on iron oxide nanoparticles for bone regeneration. ChemPhysChem 19:1965–1979. https://doi.org/10.1002/cphc.201701294
19. Guo Y, Wang M, Ge J et al (2020) Bioactive biodegradable polycitrate nanoclusters enhances the myoblast differentiation and in vivo skeletal muscle regeneration via p38 MAPK signaling pathway. Bioact Mater 5:486–495. https://doi.org/10.1016/j.bioactmat.2020.04.004
20. Lassar AB (2009) The p38 MAPK family, a pushmi-pullyu of skeletal muscle differentiation. J Cell Biol 187:941–943. https://doi.org/10.1083/jcb.200911123
21. Lluís F, Perdiguero E, Nebreda AR et al (2006) Regulation of skeletal muscle gene expression by p38 MAP kinases. Trends Cell Biol 16:36–44. https://doi.org/10.1016/j.tcb.2005.11.002
22. Lawan A, Min K, Zhang L et al (2018) Skeletal muscle-specific deletion of MKP-1 reveals a p38 MAPK/JNK/Akt signaling node that regulates obesity-induced insulin resistance. Diabetes 67:624–635. https://doi.org/10.2337/db17-0826
23. Carter CS, Huang SC, Searby CC et al (2020) Exposure to static magnetic and electric fields treats type 2 diabetes. Cell Metabol 32:561. https://doi.org/10.1016/j.cmet.2020.09.012
24. Blache U, Metzger S, Vallmajo-Martin Q et al (2016) Dual role of mesenchymal stem cells allows for microvascularized bone tissue-like environments in PEG hydrogels. Adv Healthcare Mater 5:489–498. https://doi.org/10.1002/adhm.201500795
25. Kim JH, Kim I, Seol YJ et al (2020) Neural cell integration into 3D bioprinted skeletal muscle constructs accelerates restoration of muscle function. Nat Commun 11(1):1025. https://doi.org/10.1038/s41467-020-14930-9
26. Li N, Yang L, Pan C et al (2020) Naturally-occurring bacterial cellulose-hyperbranched cationic polysaccharide derivative/MMP-9 siRNA composite dressing for wound healing enhancement in diabetic rats. Acta Biomater 102:298–314. https://doi.org/10.1016/j.actbio.2019.11.005
27. Yang Y, Qiao X, Huang R et al (2020) E-jet 3D printed drug delivery implants to inhibit growth and metastasis of orthotopic

breast cancer. Biomaterials 230:119618. https://doi.org/10.1016/j.biomaterials.2019.119618
28. Kim EC, Leesungbok R, Lee SW et al (2015) Effects of moderate intensity static magnetic fields on human bone marrow-derived mesenchymal stem cells. Bioelectromagnetics 36:267–276. https://doi.org/10.1002/bem.21903
29. Czaja WK, Young DJ, Kawecki M et al (2007) The future prospects of microbial cellulose in biomedical applications. Biomacromol 8:1–12. https://doi.org/10.1021/bm060620d
30. Cai ZW, Huang KP, Bao CY et al (2019) Precise construction of cell-instructive 3D microenvironments by photopatterning a biodegradable hydrogel. Chem Mater 31:4710–4719. https://doi.org/10.1021/acs.chemmater.9b00706
31. Naeem MA, Alfred M, Lv P et al (2018) Three-dimensional bacterial cellulose-electrospun membrane hybrid structures fabricated through in-situ self-assembly. Cellulose 25:6823–6830. https://doi.org/10.1007/s10570-018-2084-9
32. Silva PE, Maldaner V, Vieira L et al (2018) Neuromuscular electrophysiological disorders and muscle atrophy in mechanically-ventilated traumatic brain injury patients: new insights from a prospective observational study. J Crit Care 44:87–94. https://doi.org/10.1016/j.jcrc.2017.10.026
33. Wang Q, Xia Q, Wu Y et al (2015) 3D-printed atsttrin-incorporated alginate/hydroxyapatite scaffold promotes bone defect regeneration with TNF/TNFR signaling involvement. Adv Healthcare Mater 4:1701–1708. https://doi.org/10.1002/adhm.201500211
34. Shi X, Ostrovidov S, Zhao YH et al (2015) Microfluidic spinning of cell-responsive grooved microfibers. Adv Funct Mater 25:2250–2259. https://doi.org/10.1002/adfm.201404531
35. Jeon H, Simon CG Jr, Kim G (2014) A mini-review: cell response to microscale, nanoscale, and hierarchical patterning of surface structure. J Biomed Mater Res B Appl Biomater 102:1580–1594. https://doi.org/10.1002/jbm.b.33158
36. Juhas M, Abutaleb N, Wang JT et al (2018) Incorporation of macrophages into engineered skeletal muscle enables enhanced muscle regeneration. Nat Biomed Eng 2:942–954. https://doi.org/10.1038/s41551-018-0290-2
37. Kim W, Lee H, Lee J et al (2020) Efficient myotube formation in 3D bioprinted tissue construct by biochemical and topographical cues. Biomaterials 230:119632. https://doi.org/10.1016/j.biomaterials.2019.119632
38. Baht GS, Bareja A, Lee DE et al (2020) Meteorin-like facilitates skeletal muscle repair through a Stat3/IGF-1 mechanism. Nat Metabol 2:278–289. https://doi.org/10.1038/s42255-020-0184-y
39. San Emeterio CL, Olingy CE, Chu Y et al (2017) Selective recruitment of non-classical monocytes promotes skeletal muscle repair. Biomaterials 117:32–43. https://doi.org/10.1016/j.biomaterials.2016.11.021
40. Heher P, Maleiner B, Prüller J et al (2015) A novel bioreactor for the generation of highly aligned 3D skeletal muscle-like constructs through orientation of fibrin via application of static strain. Acta Biomater 24:251–265. https://doi.org/10.1016/j.actbio.2015.06.033
41. Rubio Ayala M, Syrovets T, Hafner S et al (2018) Spatiotemporal magnetic fields enhance cytosolic Ca^{2+} levels and induce actin polymerization via activation of voltage-gated sodium channels in skeletal muscle cells. Biomaterials 163:174–184. https://doi.org/10.1016/j.biomaterials.2018.02.031
42. Huang NF, Patel S, Thakar RG et al (2006) Myotube assembly on nanofibrous and micropatterned polymers. Nano Lett 6:537–542. https://doi.org/10.1021/nl060060o
43. Sempf K, Arrey T, Gelperina S et al (2013) Adsorption of plasma proteins on uncoated PLGA nanoparticles. Eur J Pharm Biopharm 85:53–60. https://doi.org/10.1016/j.ejpb.2012.11.030
44. Gillies AR, Lieber RL (2011) Structure and function of the skeletal muscle extracellular matrix. Muscle Nerve 44:318–331. https://doi.org/10.1002/mus.22094
45. Filippi M, Dasen B, Guerrero J et al (2019) Magnetic nanocomposite hydrogels and static magnetic field stimulate the osteoblastic and vasculogenic profile of adipose-derived cells. Biomaterials 223:119468. https://doi.org/10.1016/j.biomaterials.2019.119468
46. Gujjalapudi M, Anam C, Mamidi P et al (2016) Effect of magnetic field on bone healing around endosseous implants - an in-vivo study. J Clin Diagnost Res 10(10):ZF01–ZF04. https://doi.org/10.7860/JCDR/2016/21509.8666
47. Petecchia L, Sbrana F, Utzeri R et al (2015) Electro-magnetic field promotes osteogenic differentiation of BM-hMSCs through a selective action on Ca^{2+}-related mechanisms. Sci Rep 5:13856. https://doi.org/10.1038/srep13856
48. Aydin N, Bezer M (2011) The effect of an intramedullary implant with a static magnetic field on the healing of the osteotomised rabbit femur. Int Orthop 35:135–141. https://doi.org/10.1007/s00264-009-0932-9
49. Li Q, Fang Y, Wu N et al (2020) Protective effects of moderate intensity static magnetic fields on diabetic mice. Bioelectromagnetics 41:598–610. https://doi.org/10.1002/bem.22305
50. Lew WZ, Huang YC, Huang KY et al (2018) Static magnetic fields enhance dental pulp stem cell proliferation by activating the p38 mitogen-activated protein kinase pathway as its putative mechanism. J Tissue Eng Regenerat Med 12:19–29. https://doi.org/10.1002/term.2333
51. Li LK, Liu CH, Timashev P et al (2019) Biofabrication of tissue-specific extracellular matrix proteins to enhance the expansion and differentiation of skeletal muscle progenitor cells. Appl Phys Rev 6:6. https://doi.org/10.1063/1.5088726
52. Chatterjee B, Wolff DW, Jothi M et al (2016) p38 alpha MAPK disables KMT1A-mediated repression of myogenic differentiation program. Skeletal Muscle 6:28. https://doi.org/10.1186/s13395-016-0100-z
53. Chen H, Zhong J, Wang J et al (2019) Enhanced growth and differentiation of myoblast cells grown on E-jet 3D printed platforms. Int J Nanomed 14:937–950. https://doi.org/10.2147/ijn.S193624
54. Zhang J, Muri J, Fitzgerald G et al (2020) Endothelial lactate controls muscle regeneration from ischemia by inducing M2-like macrophage polarization. Cell Metabol 31:1136. https://doi.org/10.1016/j.cmet.2020.05.004
55. Yang G, Jiang F, Lu Y et al (2021) Rapid construction and enhanced vascularization of microtissue using a magnetic control method. Biofabrication. https://doi.org/10.1088/1758-5090/abe4c2